RSC Advances

PAPER

View Article Online
View Journal | View Issue

Check for updates

Cite this: *RSC Adv.*, 2020, **10**, 20155

Patterned nanofiber air filters with high optical transparency, robust mechanical strength, and effective $PM_{2.5}$ capture capability†

Jinshan Cao,[a] Zhiqiang Cheng,[*a] Lijuan Kang,[a] Meng Lin[b] and Lihao Han[*b]

Received 1st March 2020
Accepted 7th May 2020

DOI: 10.1039/d0ra01967d

rsc.li/rsc-advances

$PM_{2.5}$, due to its small particle size, strong activity, ease of the attachment of toxic substances and long residence time in the atmosphere, has a great impact on human health and daily production. In this work, we have presented patterned nanofiber air filters with high optical transparency, robust mechanical strength and effective $PM_{2.5}$ capture capability. Here, to fabricate a transparency air filter by a facile electrospinning method, we chose three kinds of patterned wire meshes with micro-structures as negative receiver substrates and directly electrospun polymer fibers onto the supporting meshes. Compared with randomly oriented nanofibers (named "RO NFs" in this paper) and commercially available facemasks, the patterned air filters showed great mechanical properties, and the water contact angles on their surfaces were about 122–143° (the water contact angle for RO NFs was 81°). In addition, the patterned nanofibers exhibited high porosity (>80%), and their mean pore size was about 0.5838–0.8686 μm (the mean pore size of RO NFs was 0.4374 μm). The results indicate that the transparent patterned air filters have the best $PM_{2.5}$ filtration efficiency of 99.99% at a high transmittance of ~69% under simulated haze pollution.

Open Access Article. Published on 27 May 2020. Downloaded on 2/9/2026 2:48:05 AM.
This article is licensed under a Creative Commons Attribution-NonCommercial 3.0 Unported Licence.

1. Introduction

Over the last decade, air quality has been deteriorating in many areas of the world.[1–4] Worldwide, ambient levels of $PM_{2.5}$ (atmospheric particulate matter with aerodynamic diameters less than or equal to 2.5 μm) continue to exceed the air quality guideline (≤10 μg m^{-3}) established by the World Health Organization (WHO); moreover, 80% of the world's population lives in polluted environments, where the levels of $PM_{2.5}$ exceed the standard value. The most recent report analysis indicated that air pollution from worldwide exposure to $PM_{2.5}$ accounts for ~6% of global all-cause deaths.[5–7] The Global Burden of Disease (GBD) analysis has pointed out that the strongest causal associations are seen between $PM_{2.5}$ pollution and cardiovascular and pulmonary and lung cancer. $PM_{2.5}$ is responsible for a substantially larger number of attributable deaths than other more well-known risk factors (such as alcohol use and physical inactivity). Furthermore, increasing evidence suggests that the highest proportion of pollution-related deaths occurs in developing countries; to date, the control and removal of PM still remain a great challenge.

With the development of nanotechnology, electrospinning has become one of the main ways to prepare nanofibrous membranes effectively because of its advantages such as simple device preparation, low cost and controllable processes. In addition, electrospun nanofibrous membranes have the advantages of small fiber diameter, high porosity, large specific area and good internal porosity connectivity.[8–12] On the other hand, electrospinning can produce a variety of nanofibers, including organic,[13] organic/inorganic and inorganic nanofibers.[14–16] Compared with the traditional mask filters, electrospun nanofibrous membranes have high filtration efficiency for submicron particles and have great application value in the field of air filtration due to their low respiratory resistance.

Recent studies have demonstrated that the electrospun air filters obtained using polyurethane,[17] polyacrylonitrile,[18] polyimide and polyamide 66 (PA66) exhibit great potential.[19,20] It is noteworthy that PA66 as a thermoplastic resin not only has better mechanical strength and hardness, but also has excellent wear resistance and chemical corrosion resistance and is mostly non-toxic. For instance, Kim *et al.*[21] fabricated electrospun polyacrylonitrile nanofibers with a $PM_{2.5}$ removal efficiency of 94.02% by surface modification *via* plasma treatment; the filter was applied as a car interior air purifier, and the long-term reproducibility of the filter was higher than that of commercial filters. Liu *et al.*[22] reported the processing of a transparent air filter for high efficiency $PM_{2.5}$ capture. It was shown that the best performance for this PAN nanofibrous membrane was achieved with a $PM_{2.5}$ filtration efficiency of 98.69% at a high

[a]College of Resources and Environment, Jilin Agricultural University, Changchun 130118, People's Republic China. E-mail: cjs4451@126.com

[b]Joint Center for Artificial Photosynthesis (JCAP), California Institute of Technology (CALTECH), Pasadena, CA, USA. E-mail: hanlihao@caltech.edu

† Electronic supplementary information (ESI) available. See DOI: 10.1039/d0ra01967d

Open Access Article. Published on 27 May 2020. Downloaded on 2/9/2026 2:48:05 AM. This article is licensed under a Creative Commons Attribution-NonCommercial 3.0 Unported Licence.

transmittance of about 77%. Moreover, they further demonstrated a fast method to fabricate electrospun transparent nanofiber membranes.

The parameters that affect the properties of nanofibrous air filters include fiber diameter distribution, fiber arrangement, cross-section morphology and pore size. Based on previous studies, for air filters, the challenge is to achieve both high optical transparency and excellent mechanical properties without compromising the filtration properties. On the premise of maintaining better filtration efficiency, air filters with high optical transparency can be used not only for personal protection, but also for decoration engineering, such as high-transmittance window screens. In the present study, we report the fabrication of patterned nanofibrous membranes with high transparency and explore their application for PM capture. The wettability, mechanical properties and transmittance of the patterned air filters were characterized and compared with those of randomly oriented nanofibers and commercial masks, and the differences were analyzed. Subsequently, we analyzed the pore size distributions and porosities of the patterned nanofibrous membranes and placed them in a simulated polluted environment to test the filtration efficiency of the air filters for $PM_{0.3-5.0}$. Additionally, the formation mechanism of the patterned nanofibrous membranes for $PM_{2.5}$ capture was investigated.

2. Experimental

2.1 Chemicals

Polyamide 66 (EPR-27, white granules) and formic acid (99%, F112036, analytical reagent) were purchased from Shenma Industrial Co., Ltd. and Shanghai Aladdin Bio-Chem Technology Co., Ltd., respectively, and these reagents were used without further purification. Iron meshes (mesh numbers of 20, 60 and 100, respectively) with various patterns, named plain weave (PW), herringbone (HB) and lozenge stria (LS), were purchased from a local supermarket, and their key parameters are listed below (Table 1).

2.2 Fabrication of nanofibrous membranes

White PA66 granules were dissolved in formic acid, and the solution was stirred for 6 h using an intelligent magnetic stirrer (ZNCL-G, China) in a 60 °C water bath. After cooling to room temperature, this precursor solution was electrospun from a programmable syringe pump at a rate of 0.5 mL h^{-1}; a voltage of 19 kV was applied between the needle (anode) and the metal mesh (cathode) at a distance of 30 cm. After 3 hours of electrospinning at room temperature (~22 °C, relative humidity ~48%), the synthesized nanofibrous membranes were dried in a vacuum oven (DZF-6050, China) at 60 °C for 24 h. After the solvent was evaporated, the membranes were peeled off from the metal mesh with tweezers and then maintained in a glass dryer.

Table 1 Key parameters of the three patterned iron meshes with different mesh numbers

Mesh number	Wire diameter (mm)	Aperture (mm)	Open porosity (%)
20	0.50	1.0	18
60	0.33	0.4	40
100	0.37	0.2	70

2.3 Characterization

The surface morphologies of the nanofibrous membranes were characterized by a Zoom-stereo microscope (ZXL-500C, China), scanning electron microscope (SEM, SHIMADZU X-550, Japan, operating voltage: 15 kV), and VHX 3D digital microscope (VHX-2000C, Keyence, Japan) stepwise. The diameter distribution of the nanofibers was determined manually from the SEM images using Nanomeasure 1.2 software as described in our previous study.

The pore sizes of the nanofibrous membranes were measured using a membrane pore size analyzer based on a bubble point method (3H-2000PB, Beishide Instrument Technology Co., Ltd). The porosity (p, %) was evaluated by a density analyzer (3H-2000TD-Y, Beishide Instrument Technology Co., Ltd). The porosity is the ratio of the volume of the internal pores in a filtration membrane to its total geometric volume, which is defined by the following equation:

$$p = \frac{V_0 - V}{V_0} \times 100\% = \left(1 - \frac{p_0}{p}\right) \times 100\% \quad (1)$$

where V_0 represents the apparent volume of the material in the natural state, and V represents the absolutely compact volume of the filtration material.

The mechanical properties of the patterned nanofibrous membranes were measured by a mechanical testing tester (WDW-X, China). During the testing process, the loading force was 5 N and the stretching speed was 2 mm min^{-1}. 5 samples with a gauge length of 25 mm in a spindle-shaped sample (50 mm × 10 mm) from the same synthesis cycle were tested, and the average strain *vs.* the stress performance was plotted.

The wettability of each nanofibrous membrane interface was measured by a contact angle analyzer (Kino SL200B, USA). The water contact angles on the samples were measured by a goniometer with a 3 μL sessile deionized water droplet (diameter: ~2 mm) falling from a height of 5 cm at room temperature. The contact angles were measured three times each, and the average results were selected to represent the wettability of the samples. The optical transparency was investigated by a UV-vis spectrophotometer (TU-1950, xenon lamp as the light source).

The PM particles used for the air filtration experiments in this study were generated by burning tobacco, as tobacco smoke contains a wide range of PM particles of various sizes. As shown in Fig. 5a and S6,† the pressure drop was calculated and read from a differential pressure gauge (AS510, Smart Sensor AS510 Pty Ltd., China), and the number of particles passing through the air filters was detected by an air particle counter (METONE 237B, USA). The $PM_{2.5}$ filtration performance was tested in a home-built closed chamber. A piece of filtration membrane was clamped at the inlet of the device to ensure that the polluted air entered the test instrument completely through the filtration membrane, while a built-in ventilator recycled the air at a velocity of

 This journal is © The Royal Society of Chemistry 2020

Open Access Article. Published on 27 May 2020. Downloaded on 2/9/2026 2:48:05 AM.
This article is licensed under a Creative Commons Attribution-NonCommercial 3.0 Unported Licence.

2.2 m s^{-1}. The concentration of $PM_{2.5}$ before filtration was detected by an external portable integrated air detector (MEF-550, Sensology, USA); the initial concentration of $PM_{2.5}$ was 600 μg cm^{-3}, which was controlled by adjusting the burning time of the tobacco before our experiment. In addition, a built-in detector (SDL-307, Nova, China) was employed to determine the $PM_{2.5}$ concentration after filtration. The time of removing $PM_{2.5}$ was counted by the external Sensology detector when the $PM_{2.5}$ concentration was reduced from 600 to 35 μg cm^{-3}.

3. Results and discussion

3.1 Electrospinning of patterned nanofibrous membranes and their growth mechanism

Electrospinning was utilized as a cost-effective fabrication method for nanofibrous membranes. As illustrated in Scheme 1(a), white PA66 granules were dissolved in formic acid as the precursor solution, and an operating voltage of 19 kV was applied at a distance of 30 cm for electrospinning. In a traditional electrospinning procedure, a rotating roller or a flat plate is used as the cathode to receive the ionized precursor solution, and a RO NF nanofibrous membrane is formed on the surface of the cathode. In this work, we designed three different patterned grids and employed each iron mesh as a cathode substrate for electrospinning. When a high voltage was applied, the precursor solution ejected from the needle became ionized and traveled to the mesh along the electrical field in a conical shape. The regularly distributed patterns attracted more precursors due to their denser electrical field lines than the pores on the mesh; subsequently, a patterned nanofibrous layer was formed on the special substrate structure.

In order to fabricate nanofibrous membranes with high optical transparency, robust mechanical strength, and effective $PM_{2.5}$ capture capability, we optimized the fiber diameter, porosity, thickness, and morphology of the nanofibers by controlling the electrospinning parameters, such as the precursor concentration, flow rate, voltage, spinning duration and spinning distance. The synthesized nanofibrous films were dried in a vacuum oven before being peeled off from the mesh (Scheme 1b). The as-prepared high-transmittance nanofibrous membranes were used for air filtration in the following experiments. Benefiting from their special patterned structures, pore sizes and controllable membrane thicknesses, our synthesized nanofibrous membranes have high optical transmittance, as presented in Scheme 1(c) (~69%, defined according to the average transmittance value in the visible range of the solar spectrum).[23]

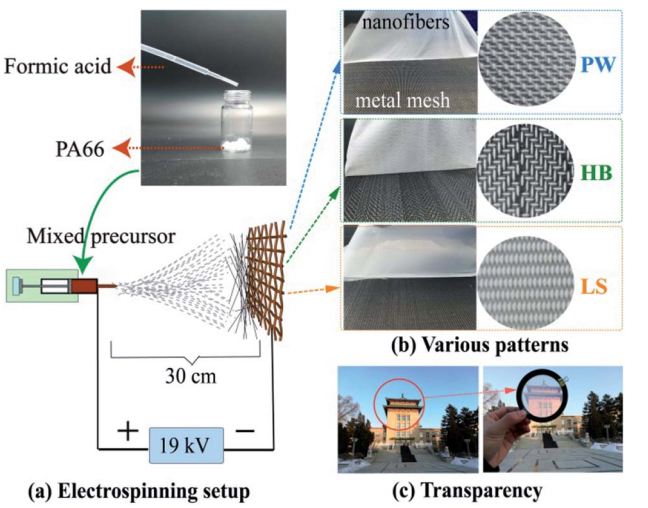

Scheme 1 (a) A schematic of the electrospinning procedure, (b) photographs of the synthesized nanofibrous membranes being peeled off from the metal meshes with various patterns, namely PW, HB and LS, and (c) the high optical transparency of the nanofibrous membranes.

Numerical simulations of the electric fields between the metal needle and the four types of patterned collectors were performed with COMSOL software (version 5.2). An electric potential of 19 kV was applied between the metal needle and a metal ground (located on the bottom of the substrate with a metal-needle-to-collector distance of 30 cm), and the collector was connected to the ground. Fig. S2† shows the distributions of the electric field for the formation processes of the various patterned nanofibrous membranes. It is known that the formation of patterned nanofibrous membranes is governed by the concentrated electric field near the collector, which attracts the highly positively charged electrospun nanofibers.[24,25] The three patterned iron mesh collectors enabled us to focus the electric field toward the collectors; as shown in Fig. S2(a–c),† the concentrated electric fields induced by the patterned metal collectors were proved to produce patterned nanofibrous membranes. In addition, a flat iron mesh collector without any pattern generated a uniformly distributed electric field (details in Fig. S2d†). The variation of the electric fields produced by using the four metal collectors can be further found through the corresponding distributions of the potential.

The distributions of the electric field between the metal needle and the grounded collectors were obtained from numerical simulations (shown in Fig. S2†). The distributions of the electric streamlines of the RO NFs and the various patterned nanofibrous membranes do not overlap obviously, and the formation of the patterned nanofibers is controlled by a concentrated electric field near the collector which attracts the highly positively charged electrospun nanofibers, based on previous studies.

3.2 Morphologies and fiber diameter distributions of the fibrous membranes

RO NFs were synthesized by the same method but using a traditional flat plate as the cathode for comparison in this work, and the electrospinning conditions were kept exactly the same as when synthesizing the three patterned nanofibrous membranes (applied voltage: 19 kV, the distance from the electrospinning needle to the substance: 30 cm) except for using different cathode meshes. The morphologies of the four samples, RO, PW, HB and LS, were characterized using a Zoom-stereo optical microscope (Column i in Fig. 1), a 3D digital microscope (Fig. S1†) and a scanning electron microscope (SEM, Column ii in Fig. 1) on different scales, and the fiber diameter distributions (Column iii in Fig. 1) were analyzed

Open Access Article. Published on 27 May 2020. Downloaded on 2/9/2026 2:48:05 AM.
This article is licensed under a Creative Commons Attribution-NonCommercial 3.0 Unported Licence.

according to the corresponding SEM images. As depicted in the first row in Fig. 1, the RO NFs had an average diameter of 190.4 nm and were distributed randomly, forming a membrane without any pattern. However, all the other three samples formed particular patterns (Fig. 1b, c and d–i) which were similar to their mesh patterns, respectively.

The average fiber diameters of the PW, HB and LS patterned nanofibers were about 133.2 nm, 151.2 nm and 118.8 nm, respectively, which are all smaller than that of the RO NFs. The stems and nodes on the patterned iron grids have stronger effects on the electrical field than the hollow parts of the substrates, and a mutually repulsive electrical field was formed around one pattern due to the polarization of stems and the single hole. The uneven electrical field distribution stretched the nanofibers during the synthesizing procedure; therefore, the nanofibers deposited onto the patterned substrates were usually thinner than the RO NFs, whose electrical field was more uniformly distributed on the substrate. This smart design of patterned nanofibrous membranes on the nanoscale has advantages in improving the mechanical strength of the membrane and filtration efficiency while keeping the membrane optically transparent on the macroscopic scale.[26] These improvements will be explored later in this paper.

3.3 Mechanical strength, pore structure and anti-wettability

Mechanical strength is critical for the life expectancy of nanofibrous membranes if they are employed for practical air filter

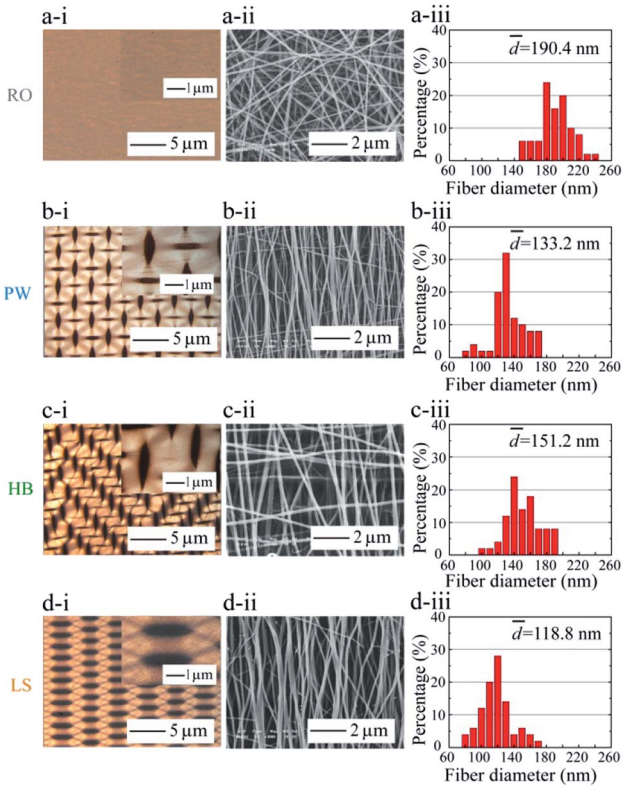

Fig. 1 (i) Photomicrographs, (ii) SEM images and (iii) fiber diameter distributions of various nanofibrous membranes with different patterns: (a) RO NFs; (b) PW NFs; (c) HB NFs and (d) LS NFs.

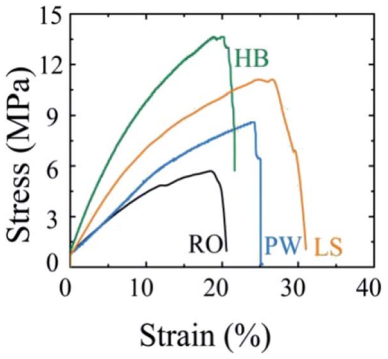

Fig. 2 Stress–strain responses of nanofibrous membranes.

applications. As shown in Fig. 2, the nanofibrous membranes showed nonlinear elastic deformation under the initial tensile force. This is mainly because the nanofibers are forced to orientate along the direction of stress under the action of tensile force until breakage of the membranes occurs due to the fracture of a single nanofiber. Significantly, all the patterned nanofibrous membranes have better tensile strength (>6.63 MPa) and elongation at break (>21.65%). For instance, the strain and stress of the HB NFs were about 31.04% and 11.09 MPa, respectively. By contrast, the RO NFs exhibited a tensile strength of 5.69 MPa and a strain at break of approximately 21%. Moreover, we investigated the mechanical properties of three patterned NFs with different mesh numbers (details in Fig. S4†). Compared with RO NFs, the elongation at break of the patterned fibrous membranes increased with increasing mesh number; this indicates that the denser the microstructure, the stronger the mechanical properties of the formed nanofibrous membranes. These results fully demonstrate that the patterned NFs have sufficient mechanical properties for air filtration in practical applications.

The pore structure, size distribution and porosity of nanofibrous membranes play important roles in determining their gas permeation rate and moisture permeability, thus affecting the air resistance at a certain pore size.[27,28] Particularly, the minimum and average pore sizes are the key parameters that affect the PM physical trapping capabilities, which have the most straightforward effect on the filtration efficiency. In this work, the pore size distributions and porosities of the four types of nanofibrous membranes were respectively characterized. The pore size distributions of the patterned nanofibrous membranes are more extensive and their pore sizes are larger than those of the RO NFs (as shown in Fig. 3a and Fig. S3†). The results in Fig. 3(a and b) show that the average pore sizes of the PW, HB and LS NFs are about 0.5838, 0.6658 and 0.8686 μm, respectively; however, the RO NFs have an average pore size of 0.4374 μm. Additionally, the minimum pore sizes of the patterned NFs are larger than that of the RO NFs. The most obvious reason for this is that the patterned NFs were more likely to be electrospun across/along the pores of the patterned metal mesh and form a large number of structures during the aggregation process. In addition, from Fig. 3b, the porosities of the patterned nanofibrous membranes are 85.3%, 83.0% and

 This journal is © The Royal Society of Chemistry 2020

Open Access Article. Published on 27 May 2020. Downloaded on 2/9/2026 2:48:05 AM.
This article is licensed under a Creative Commons Attribution-NonCommercial 3.0 Unported Licence.

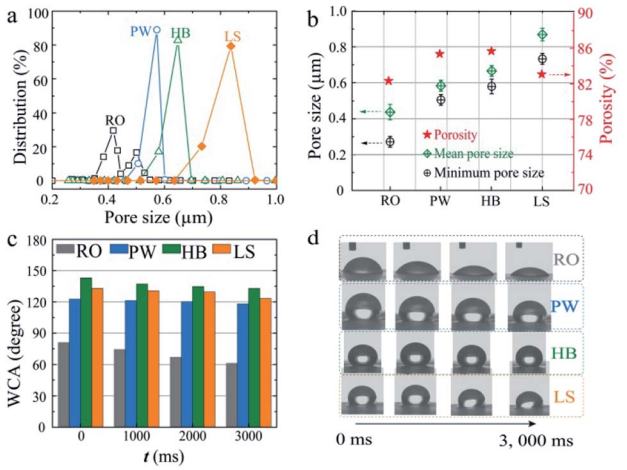

Fig. 3 (a) Pore size distribution analysis of the nanofibrous membranes. (b) Mean pore sizes and minimum pore sizes of the various nanofibrous membranes and their corresponding porosities. (c) Variations of the water contact angles with time from 0 to 3000 ms for the surfaces of the RO NFs and the various patterned nanofibrous membranes. (d) The corresponding optical microscope images showing changes of the contact angles with time, recorded by a CCD camera at 0 ms, 1000 ms, 2000 ms and 3000 ms.

86.8%, respectively, while that of the RO NFs is 82.3%. From the above results, the pore size distributions and porosities of the patterned nanofibers are generally larger than those of the RO NFs, which is beneficial to the optical transparency, gas and moisture permeability of air filters in further application.

The phenomenon in which a liquid can expand on a solid surface is called wetting behavior, and the contact angle measured using deionized water as a liquid is called the water contact angle. Moreover, excellent wettability will help to improve the self-cleaning of fibrous membranes so that the air filters can maintain great filtration performance in a wet environment. Fig. 3c and d show the wetting behaviors of water on the surface of the nanofibrous membranes. The results show that the patterned nanofibrous membranes showed excellent hydrophobicity; the water contact angles were about 122–143°, compared with 81° for the RO sample, in the beginning of the test. Subsequently, the water contact angles for the surfaces of the patterned nanofibrous membranes remained basically unchanged with time from 0 to 3000 ms compared to the RO NFs (Fig. 3d). Previous research confirmed that wettability can be formed by graded micro-nanostructures on the surface of materials.[29] Therefore, these results show that the micro-patterned structures on the surfaces of the nanofibrous membranes greatly change their hydrophobic properties and wetting behavior.

3.4 Transmittance of the patterned nanofibrous membranes

Generally, the wavelengths of electromagnetic waves that the human eye can sense are between 380-780 nm. In order to more intuitively show that the patterned nanofibrous membranes have excellent optical transparency, we integrated the LS NFs in the wing of a dragonfly model. We found that the patterned nanofibrous membranes exhibit high optical transparency (Fig. 4a). Furthermore, to make the as-prepared filtration membranes more suitable for practical application, we used a fan to simulate a windy environment and tested the air permeability and wind resistance of the air filters. The results show that the nanofibrous membranes at a high transmittance of ~69% have excellent mechanical properties and air permeability (the air velocity was controlled at 2.5 m s^{-1} (Fig. 4b). We prepared patterned nanofibrous membranes with membrane thicknesses of 4 μm, 8 μm, and 16 μm, and the transmittances of the same patterns with different thicknesses were compared (Fig. S5†). The average transmittances of the PW, HB and LS NFs with a thickness of 4 μm over the visible region are about 69%, 65%, and 59%, respectively (Fig. 4c). In addition, by comparing the transmittance of HB NFs with different thicknesses (Fig. 4d), we found that the light transmittance of the NFs is closely related to the membrane thickness; the thinner the fibrous membrane, the better the light transmittance. As a result, for the different mesh numbers (Fig. 4e), the HB NFs (mesh number 100) have better light transmittance. According to the results of previous research, the internal light loss is mainly due to light scattering between the gaps of the nanofibers, and the surface reflection is caused by the different refractive indices of air and the air filter.[30,31]

3.5 Air filtration performance

Based on the above results, the patterned NFs prepared in this paper have excellent optical transparency and robust mechanical properties; however, their removal efficiency for PM is not known. To confirm that the three patterned NFs also have excellent filtration performance, the $PM_{2.5}$ capture capabilities of the as-electrospun patterned nanofibers were tested using reactors (Fig. 5a and S6†). Fig. 5a shows a photograph of the pressure drop measurement, in which the pressure difference across the air filter was monitored. The nanofibrous

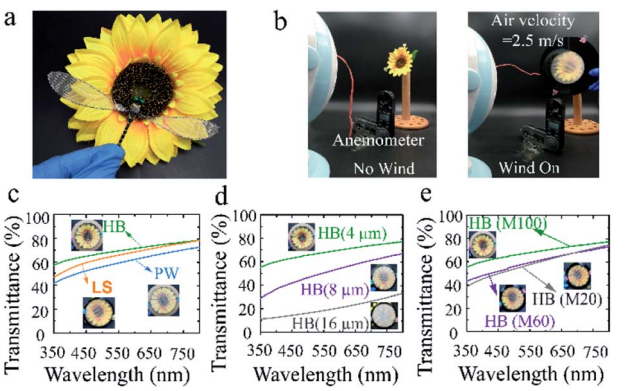

Fig. 4 (a) The as-prepared transparent air filter was integrated in the wing of a dragonfly model to observe its transmittance in front of a cloth sunflower. (b) Photographic images of the transparent patterned air filters with an electric fan at air velocity of 2.5 m s^{-1}. (c) Optical transmittances in the visible light wavelength range of the various fibrous membranes with a thickness of 4 μm. (d) Light transmittance of HB NFs with different membrane thicknesses and (e) different mesh numbers (measurement wavelength range: 300–800 nm). The insets are the corresponding digital images.

Open Access Article. Published on 27 May 2020. Downloaded on 2/9/2026 2:48:05 AM.
This article is licensed under a Creative Commons Attribution-NonCommercial 3.0 Unported Licence.

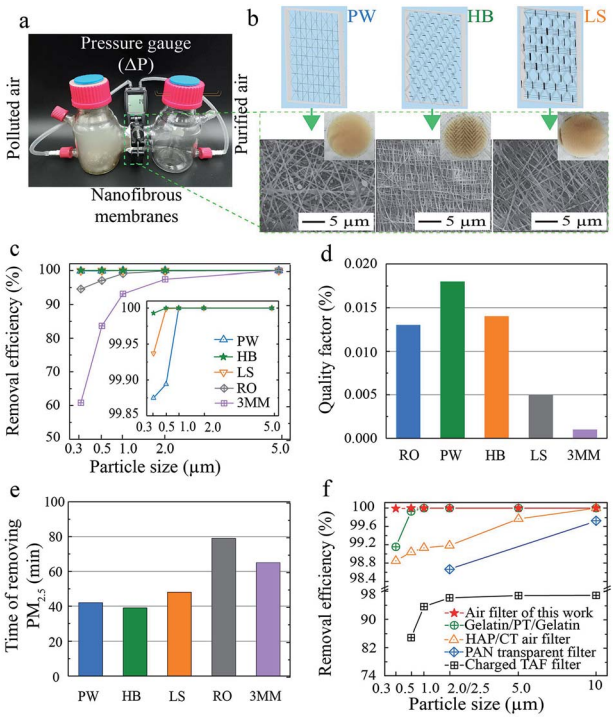

Fig. 5 (a) The air filtration experiment setup. (b) Optical images of $PM_{2.5}$ filtration processes over the patterned nanofibrous membranes in a simulated haze environment. (c) Comparison of removal efficiency and (d) quality factors between various patterned fibrous membranes, randomly oriented fibrous membranes and a commercial face mask. (e) Time to remove $PM_{2.5}$ from about 600 to 35 μg cm^{-3} (temperature of 18 °C and humidity of 45%; the air velocity was 2.2 m s^{-1}). (f) Comparison of removal efficiency between the current HB patterned air filter and other reported air filters: gelatin/PT/gelatin air filter,[32] HAP/CT air filter,[33] PAN transparent air filter[22] and charged TAF air filter.[34]

membranes were clamped gas-tightly in the middle of an H-shaped cell. The left side simulates polluted air with burning tobacco, while the right side contains purified air. Furthermore, the filtration performance of nanofibrous membranes for $PM_{2.5}$ was tested in the simulated polluted air environment; here, we demonstrate a schematic of the patterned NFs that capture PM particles. Additionally, the obtained patterned nanofibrous membranes were used as air filters to capture PM particles and measure the air particle index for one day; the three patterned air filters based on nanofibers have attractive attributes of high filtration efficiency for polluted air in a simulated haze environment, as shown in Fig. 5b.

The filtration efficiency of the air filters for PM was calculated by the following formula, and the results are shown in Fig. 5c and Table 2.

$$\eta = \frac{C_{in} - C_{out}}{C_{in}} \times 100\% \quad (2)$$

where C_{in} and C_{out} represent the cumulative mass concentration of particles at the inlet and outlet, respectively. Among these, the removal efficiencies for $PM_{0.3}$ of the PW NFs, HB NFs and LS NFs were 99.875%, 99.993%, and 99.937% respectively, and the corresponding pressure drops (ΔP) were about 499, 521 and 518 Pa. By contrast, the filtration efficiencies of the RO NFs and commercial face masks (9501C, 3M China) were only 94.572% and 60.748%, respectively. We can find that the patterned nanofibrous air filters showed higher filtration efficiency than the RO NFs. Additionally, the corresponding pressure drops were about 533 Pa and 869 Pa, respectively. The pressure difference between the upstream air inflow side and the downstream air outflow side of an air filter becomes the pressure drop under the rated air volume. The pressure drop will increase with increasing dust accumulation inside the air filter in actual use. The overall performance of nanofibrous air filters is assessed by the quality factor (QF). The quality factor is expressed by the following equation.

$$QF = \frac{\ln(1-\eta)}{\Delta P} \times 100\% \quad (3)$$

Here, η represents the removal efficiency for PM and ΔP represents the pressure drop. The higher the quality factor, the better the comprehensive filtration performance of air filters. As observed in Fig. 5d, the quality factors of the PW, HB and LS NFs were 0.013, 0.018 and 0.014, respectively, while those of the RO NFs and a commercial 3MM mask were 0.005 and 0.001, respectively.

In order to test the filtration performance of the nanofiber air filters for $PM_{2.5}$ in practical application, the time required for the concentration of $PM_{2.5}$ to decrease from 600 to 35 μg cm^{-3} in a closed environment was measured to characterize the purification rates of the air filters (Fig. 5e). Because the patterned nanofiber air filter in this work (HB) has the advantages of high efficiency and low-pressure resistance, it only needed 36 min to realize efficient purification of air. However, 79 min and 65 min were required to purify the air for RO NFs and the commercial face mask, respectively. These results show that the patterned NFs have an excellent purification rate for $PM_{2.5}$.

Table 2 Detailed data of nanofibrous membranes for filtration of airborne particles

	Filtration efficiency (%)							
Sample	0.3 μm	0.5 μm	1.0 μm	2.0 μm	5.0 μm	ΔP/Pa	QF	Thickness/mm
PW	99.875	99.894	100	100	100	499 ± 3	0.013	0.020 ± 0.004
HB	99.993	100	100	100	100	521 ± 2	0.018	0.015 ± 0.002
LS	99.937	99.999	100	100	100	518 ± 2	0.014	0.012 ± 0.002
RO	94.572	97.125	99.142	99.864	100	533 ± 2	0.005	0.015 ± 0.003
3M face mask	60.827	83.625	93.136	97.481	99.991	869 ± 4	0.001	1.258 ± 0.005

This journal is © The Royal Society of Chemistry 2020

Open Access Article. Published on 27 May 2020. Downloaded on 2/9/2026 2:48:05 AM.
This article is licensed under a Creative Commons Attribution-NonCommercial 3.0 Unported Licence.

Finally, we compared the filtration efficiency of the patterned nanofibrous membranes in the current work with other reported air filters. In these reported air filters, a similar condition was that the removal efficiency for $PM_{0.3\text{-}10}$ was tested. As can be seen from Fig. 5f, the patterned HB NFs in this work can maintain high filtration efficiency (>99.99%) for small particle sizes (0.3 μm). The filtration efficiency of the patterned HB NFs was slightly higher than those of other air filters.

4. Conclusions

In summary, we provide a facile design to fabricate transparent nanofibrous air filters with controllable designed patterns and appropriate pore sizes for $PM_{2.5}$ capture. The results indicated that the morphologies and pore sizes of the patterned air filters can be finely controlled by using iron meshes with different micro-nanostructures. Furthermore, for the patterned NFs with transmittance of about 69%, sufficient light can penetrate through, including light from the sun. It was also found that all the patterned air filters exhibit high hydrophobicity and better mechanical properties than RO NFs. The transparent air filters showed great filtration efficiency (maintained above 99.99%) for $PM_{0.3}$; thus, they have great potential in air filtration.

Conflicts of interest

There are no conflicts to declare.

Acknowledgements

This work is supported by Jilin Province Innovation Capacity Building Fund Project (2019C050-9), Jilin Provincial Department of Science and Technology Natural Science Foundation (20180101212JC) and Changchun Science and Technology Project (18DY023).

Notes and references

1 J. Xu, C. Liu, P. C. Hsu, K. Liu, R. Zhang, y. Liu and Y. Cui, *Nano Lett.*, 2016, **16**, 1270–1275.
2 Q. Zhang, X. Jiang, D. Tong, S. J. Davis, H. Zhao, G. Geng, T. Feng, B. Zheng, Z. Lu, D. G. Streets, R. Ni, M. Brauer, A. V. Donkelaar, R. V. Martin, H. Huo, Z. Liu, D. Pan, H. Kan, Y. Yan, J. Lin, K. He and D. Guan, *Nature*, 2017, **543**, 705–709.
3 A. Talbi, Y. Kerchich, R. Kerbachi and M. Boughedaoui, *Environ. Pollut.*, 2018, **232**, 252–263.
4 X. Zhang, W. Zhang, M. Yi, Y. Wang, P. Wang, J. Xu, F. Niu and F. Lin, *Sci. Rep.*, 2018, **8**, 4757.
5 A. V. Donkelaar, R. V. Martin, M. Brauer, R. Kahn, R. Levy, C. Verduzco and P. J. Villeneuve, *Environ. Health Perspect.*, 2010, **118**, 847–855.
6 J. S. Apte, J. D. Marshall, A. J. Cohen and M. Brauer, *Environ. Sci. Technol.*, 2015, **49**, 8057–8066.
7 J. Lelieveld, A. Haines and A. Pozzer, *Lancet Planet. Health*, 2018, **2**, e292–e300.
8 D. Li and Y. Xia, *Adv. Mater.*, 2004, **16**, 1151–1170.
9 A. Greiner and J. H. Wendorff, *Angew. Chem., Int. Ed.*, 2007, **46**, 5670–5730.
10 P. Wen, M. Zong, R. J. Linhardt, K. Feng and H. Wu, *Trends Food Sci. Technol.*, 2017, **70**, 56–68.
11 C. Drosou, M. Krokida and C. G. Biliaderis, *Food Hydrocoll.*, 2018, **77**, 726–735.
12 A. Haider, S. Haider and I. K. Kang, *Arabian J. Chem.*, 2018, **11**, 1165–1188.
13 G. Sargazi, D. Afzali, A. Mostafavi and S. Y. Ebrahimipour, *J. Polym. Environ.*, 2018, **26**, 1804–1817.
14 G. Yang, W. Yan, Q. Zhang, S. Shen and S. Ding, *Nanoscale*, 2013, **5**, 12432–12439.
15 N. Qin, J. Xiong, R. Liang, Y. Liu, S. Zhang, Y. Li, Z. Li and L. Wu, *Appl. Catal. B Environ.*, 2017, **202**, 374–380.
16 P. Wang, L. Cheng, Y. Zhang and L. Zhang, *J. Alloys Compd.*, 2017, **716**, 306–320.
17 C. Yao, X. Li, K. G. Neoh, Z. Shi and E. T. Kang, *J. Membr. Sci.*, 2008, **320**, 259–267.
18 F. Mehrpouya, J. Foroughi, S. Naficy, J. M. Razal and M. Naebe, *Nanomaterials*, 2017, **7**, 293.
19 Y. E. Miao, G. N. Zhu, H. Hou, Y. Y. Xia and T. Liu, *J. Power Sources*, 2013, **226**, 82–86.
20 X. Guan, G. Zheng, K. Dai, C. Liu, X. Yan, C. Shen and Z. Guo, *ACS Appl. Mater. Interfaces*, 2016, **8**, 14150–14159.
21 H. J. Kim, S. J. Park, C. S. Park, T. H. Lee, T. H. Ha, H. Kim, J. Kim, C. S. Lee, H. Yoon and O. S. Kwon, *Chem. Eng. J.*, 2018, **339**, 204–213.
22 C. Liu, P. C. Hsu, H. W. Lee, M. Ye, G. Zheng, N. Liu, W. Li and Y. Cui, *Nat. Commun.*, 2015, **6**, 6205.
23 H. Gu and T. M. Swager, *Adv. Mater.*, 2008, **20**, 4433–4437.
24 D. Li, G. Ouyang, J. T. McCann and Y. Xia, *Nano Lett.*, 2005, **5**, 913–916.
25 D. Zhang and J. Chang, *Adv. Mater.*, 2007, **19**, 3664–3667.
26 S. Zhang, W. S. Shim and J. Kim, *Mater. Des.*, 2009, **30**, 3659–3666.
27 M. Khayet, A. Velázquez and J. I. Mengual, *J. Non-Equilib. Thermodyn.*, 2004, **29**, 279–299.
28 C. Feng, K. C. Khulbe, T. Matsuura, S. Tabe and A. F. Ismail, *Sep. Purif. Technol.*, 2013, **102**, 118–135.
29 K. Liu, X. Yao and L. Jiang, *Chem. Soc. Rev.*, 2010, **39**, 3240–3255.
30 Y. L. Huang, A. Baji, H. W. Tien, Y. K. Yang, S. Y. Yang, C. M. Ma, H. Y. Liu, Y. W. Mai and N. H. Wang, *Nanotechnology*, 2011, **22**, 475603.
31 Y. Liu, Y. Liu, J. H. Lee, C. Lee, M. Park and H. Y. Kim, *Compos. Sci. Technol.*, 2015, **117**, 404–409.
32 H. Souzandeh, L. Scudiero, Y. Wang and W. H. Zhong, *ACS Sustainable Chem. Eng.*, 2017, **5**, 6209–6217.
33 Z. C. Xiong, R. L. Yang, Y. J. Zhu, F. F. Chen and L. Y. Dong, *J. Mater. Chem. A*, 2017, **5**, 17482–17491.
34 Y. Bai, C. B. Han, C. He, G. Q. Gu, J. H. Nie, J. J. Shao, T. X. Xiao, C. R. Deng and Z. L. Wang, *Adv. Funct. Mater.*, 2018, **28**, 1706680.